

# Charge-Transfer Regulated Visible Light Driven Photocatalytic H<sub>2</sub> Production and CO<sub>2</sub> Reduction in Tetrathiafulvalene Based Coordination Polymer Gel

**Parul Verma**

Jawaharlal Nehru Centre for Advanced Scientific Research

**Pallavi Sarkar**

Jawaharlal Nehru Centre for Advanced Scientific Research

**Ashish Singh**

Jawaharlal Nehru Centre for Advanced Scientific Research

**Swapan Pati**

JNCASR

**Tapas Maji** (✉ [tmaji@jncasr.ac.in](mailto:tmaji@jncasr.ac.in))

Jawaharlal Nehru Centre for Advanced Scientific Research

---

## Article

**Keywords:** Soft Processable Metal-Organic Hybrid Semiconducting Material, Tetrapodal Low Molecular Weight Gelator

**Posted Date:** November 9th, 2020

**DOI:** <https://doi.org/10.21203/rs.3.rs-96702/v1>

**License:**  This work is licensed under a Creative Commons Attribution 4.0 International License.

[Read Full License](#)

---

**Version of Record:** A version of this preprint was published at Nature Communications on December 1st, 2021. See the published version at <https://doi.org/10.1038/s41467-021-27457-4>.

# Abstract

The much-needed renewable alternatives to fossil fuel can be achieved efficiently and sustainably by converting solar energy to solar fuels via hydrogen generation from water or CO<sub>2</sub> reduction. In this regard, a soft processable metal-organic hybrid semiconducting material has been developed and studied for photocatalytic activity towards H<sub>2</sub> production and CO<sub>2</sub> reduction to CO and CH<sub>4</sub> under visible light and direct sunlight irradiation. A tetrapodal low molecular weight gelator is synthesized by integrating tetrathiafulvalene and terpyridine through amide linkage (TPY-TTF). The TPY-TTF acts as a linker and by self-assembly with ZnII results in a charge-transfer (CT) coordination polymer gel (CPG); Zn-TPY-TTF. The Zn-TPY-TTF shows impressive photocatalytic activity towards H<sub>2</sub> production (rate = 530 μmol g<sup>-1</sup>h<sup>-1</sup>) and CO<sub>2</sub> reduction to CO (rate = 438 μmol g<sup>-1</sup>h<sup>-1</sup>, selectivity >99%) regulated by charge-transfer interaction. Furthermore, in-situ stabilization of Pt nanoparticles to CPG (Pt@Zn-TPY-TTF) exhibits remarkably enhanced H<sub>2</sub> evolution (rate = 14727 μmol g<sup>-1</sup>h<sup>-1</sup>). Importantly, Pt@Zn-TPY-TTF modulate the CO<sub>2</sub> reduction from CO to CH<sub>4</sub> (rate = 292 μmol g<sup>-1</sup>h<sup>-1</sup>, selectivity >97%). Real-time CO<sub>2</sub> reduction reaction is monitored by in-situ DRIFT study and subsequent plausible mechanism is derived computationally. The photocatalytic activity of Zn-TPY-TTF and Pt@Zn-TPY-TTF composite was also examined under sunlight that display excellent H<sub>2</sub> evolution and CO<sub>2</sub> reduction.

# Introduction

Artificial photosynthesis, i.e., the conversion of sunlight into fuels, is a green approach and has the potential to solve the global energy crisis. In recent years, a significant amount of research has been carried out to develop artificial systems for mimicking the sophisticated methodology of nature's water splitting<sup>1-4</sup> as well as CO<sub>2</sub> reduction.<sup>5-8</sup> Natural photosynthesis (NPs) rely on the occurrence of precise sequences of protein/enzymes to the several elementary steps of intercomponent light-absorbing, charge separation, and migration.<sup>9,10</sup> The synthetic assimilation of these parameters precisely in a spatial organization of molecular components is indeed a challenging task.<sup>11-14</sup> The recent upsurge of converting CO<sub>2</sub> into fuels like CH<sub>3</sub>OH, CH<sub>4</sub>, or different chemical feedstock has gained widespread attention.<sup>15-19</sup> The conversion of CO<sub>2</sub> to hydrocarbon fuels would mitigate not only the effect of CO<sub>2</sub> concentration in the atmosphere but also reduce the dependency on fossil fuel-based economy. However, the photoreduction of CO<sub>2</sub> molecules is a complex and challenging process due to the very high dissociation energy of the C=O bond (~750 kJ/mol).<sup>20</sup> Only a handful of metal<sup>21-23</sup>, metal oxide<sup>24-26</sup>, and chalcogenides<sup>27,28</sup> based heterogeneous catalysts reported for photocatalytic CO<sub>2</sub> reduction to CH<sub>4</sub>, but most of them suffer from a low conversion efficiency and poor selectivity.<sup>29</sup> CH<sub>4</sub> formation is thermodynamically favourable ( $E^0 = -0.24$  V versus RHE at pH=7) than CO formation ( $E^0 = -0.53$  V versus RHE at pH=7)<sup>30,31</sup> as the former reaction takes place at a lower potential. Nevertheless, from a kinetic point of view, the eight-electron reduction of CO<sub>2</sub> to CH<sub>4</sub> is more difficult especially under photochemical condition than the two-electron reduction of CO<sub>2</sub> to CO.<sup>32</sup> To address challenges associated with photochemical H<sub>2</sub> production and CO<sub>2</sub> reduction, a novel photocatalytic system needs to be developed by

the innovative design of photosensitizer and catalytic moiety.<sup>33,34</sup> Recently, carbon-nitride based photocatalyst for H<sub>2</sub> evolution and CO<sub>2</sub> reduction to CO has been reported.<sup>35</sup> Moreover, there is a huge lacuna in designing and developing such versatile photocatalyst materials that can reduce both, water and CO<sub>2</sub> efficiently.

To this end, developing soft hybrid materials such as coordination polymer gel (CPGs), assembled by the low molecular weight gelator (LMWG) based linker and suitable metal ions, could be an excellent design approach in the realm of photocatalysis.<sup>36-39</sup> Such hierarchical soft nano-fibrous materials<sup>40,41</sup> can facilitate the facile diffusion of reactants to the active sites and thus, will have the potential to overcome the low charge mobility and also ease efficient electron transfer between the different components.<sup>42-44</sup> These artificial hybrid synthetic systems can mimic the intricate functioning of natural photosystem and can eventually show impressive H<sub>2</sub> evolution from water<sup>45-48</sup> or CO<sub>2</sub> reduction. Extended, face-to-face array of the donor-acceptor<sup>46</sup>  $\pi$ -chromophoric system would be an ideal candidate for light-harvesting.<sup>49</sup> These systems will allow greater exciton mobility, which, in turn, leads to charge generation and subsequent electron transfer to the catalyst. To this end, tetrathiafulvalene (TTF) moiety is a well-known p-type<sup>50</sup> semiconductor possessing high electron donation capability with excellent photostability and good charge carrier mobility. Further, integration of a suitable electron acceptor unit to the TTF moiety could result in a system with excellent charge transfer characteristics.<sup>51</sup> Thus, designing a TTF containing donor-acceptor<sup>52,53</sup> based low molecular weight gelator (LMWG) could be an elegant approach for developing new photocatalyst material. Such systems are likely to show low energy charge transfer in the visible range which will further reduce the bandgap and corresponding visible light photocatalyst can be realized. Coordination driven array of donor-acceptor pairs would further improve photocatalytic performances by enhancing charge-transfer to the catalytic centre. Thus, the introduction of a suitable metal-binding moiety like terpyridine on TTF containing LMWG could lead to the formation of coordination polymer gel (CPG) and provide an opportunity for further improving the photocatalytic activity.

In this work, we aimed to report an emerging class of materials known as 'coordination polymer gel' by integrating Zn<sup>II</sup> with TTF based LMWG and explored as a photocatalyst system for solar fuel production based on water and CO<sub>2</sub> reduction. The intermolecular charge transfer was regulated by the innovative design of LMWG where TTF core was connected with metal binding TPY through a flexible alkyl amide chain. The coordination polymer gel (Zn-TPY-TTF) provides a suitable platform for light harvesting as well as a catalytic center for H<sub>2</sub> production from water (530  $\mu\text{mol g}^{-1}\text{h}^{-1}$ ) and CO<sub>2</sub> reduction to CO (438  $\mu\text{mol g}^{-1}\text{h}^{-1}$ ) with 99% selectivity. Furthermore, Zn-TPY-TTF CPG with nanofiber morphology was conjugated with Pt co-catalyst, and the composite Pt@Zn-TPY-TTF showed many folds enhanced photocatalytic activity towards H<sub>2</sub> production (14727  $\mu\text{mol g}^{-1}\text{h}^{-1}$ ). Interestingly, this composite dramatically changed the CO<sub>2</sub> reduction product to CH<sub>4</sub> (292  $\mu\text{mol g}^{-1}\text{h}^{-1}$ ) with high selectivity (97%) and impressive quantum efficiency. Importantly, both Zn-TPY-TTF and Pt@Zn-TPY-TTF showed the potential to perform sunlight driven photocatalytic activity under ambient conditions. We have also validated the

crucial role of charge transfer of the CPG in the photocatalysis and elucidated the mechanism of water and CO<sub>2</sub> reduction, respectively, through the in-situ DRIFT study and DFT calculation. To the best of our knowledge, this is the first report on the exploration of coordination polymer gels as a photocatalyst for water and CO<sub>2</sub> reduction under visible light as well as direct sunlight irradiation.

## Results

The TPY-TTF LMWG was synthesized by the amide coupling reaction between 2,2':6',2''-terpyridin-4-yl-propane-1,3-diamine (TPY-NH<sub>2</sub>)<sup>54</sup> and 1,3,6,8-tetrakis (benzoic acid) tetrathiafulvalene (TTF(COOH)<sub>4</sub>)<sup>55</sup> (details are given in supporting information (SI)), Supplementary Fig. 1-2). The newly synthesized TPY-TTF LMWG was characterized by NMR, Mass, FT-IR (Supplementary Figs. 3-6). UV-Vis absorption study was performed for a well-characterized TPY-TTF LMWG in methanol. 10<sup>-6</sup> M methanolic solution of TPY-TTF showed distinguished absorption bands at 270 nm and 320 nm corresponding to the π@π\* transition for TPY unit and TTF core, respectively (Fig. 1c). Notably, a low energy absorption band appeared at 520 nm that can be ascribed to intramolecular charge transfer (CT) interaction between TTF core and benzo-amide moiety.<sup>55</sup> The CT property of TPY-TTF has also been supported by density functional theoretical (DFT) computation where highest occupied molecular orbital (HOMO), and lowest unoccupied molecular orbital (LUMO) is centered in TTF and benzo-amide groups, respectively (Fig. 3b).

Next, we have examined gelation propensity of TPY-TTF LMWG in several solvent compositions (see the SI). Notably, heating the solution of TPY-TTF in MeOH/DCM/H<sub>2</sub>O (2:1:1) at 60 °C followed by cooling to room temperature (rt) resulted in a purple coloured opaque gel (TPY-TTF OG) (Supplementary Figs. 7-8). Further, the formation of the gel was confirmed by the inversion test method (Fig. 1a). Morphology of the TPY-TTF xerogel was recorded by the Atomic Force Microscopy (AFM) and Field Emission Scanning Electron Microscopy (FE-SEM) that showed micron size staked layered type of morphology (Fig. 1e-1f). Transmission Electron Microscopy (TEM) images have further confirmed such morphologies (Fig. 1g). Powder X-ray diffraction (PXRD) study of the TPY-TTF xerogel showed a peak at 2θ = 24° with a d-spacing of 3.7 Å, indicating that the self-assembly was driven by intermolecular π-π stacking interactions (Fig. 1d). Further, high-resolution TEM image showed the ordering with the lattice fringes at 3.7 Å, also suggesting π-π interactions formed 2D stacking of layers (Fig. 1b, 1g: inset). The UV-Vis absorption study for TPY-TTF xerogel displayed slightly red-shifted absorption as compared to the methanolic solution of TPY-TTF LMWG (Fig. 1c). It showed absorption bands at 300 nm and 330 nm, which can be assigned for π@π\* transitions of terpyridine and TTF units, respectively. Notably, a broad absorption between 520-560 nm was also observed, indicating the existence of CT in TPY-TTF in xerogel state. The optical band gap for TPY-TTF OG calculated by the Kubelka-Munk plot derived from UV-vis diffuse reflectance spectrometry was found to be 2.26 eV (Supplementary Fig. 9). The experimental band gap was further supported by performing density functional theory calculations on simplified models of TPY-TTF OG systems (Fig. 3a). The TD-DFT calculations have indicated that the intramolecular charge transfer transition took place at wavelength 540 nm in TPY-TTF OG from donor TTF core to acceptor -PhCONH<sub>2</sub> moiety (Fig. 3b and Supplementary Fig. 10). The intermolecular distance between TTF and

terpyridine moiety in the TPY-TTF OG was estimated theoretically and found to be 3.558 Å which indicates for the feasibility for the intermolecular CT as well (Fig. 3a). The computed results suggested the intramolecular charge transfer contribute much significantly (47%) compared to the weak intermolecular charge transfer process (1.3%). Thus, the results revealed that the visible light absorption in the TPY-TTF OG is mainly attributed to the intramolecular CT rather than intermolecular CT process. Next, the presence of four terpyridine units in the TPY-TTF gelator has prompted us to investigate further their metal-binding ability to develop coordination polymer gel (CPG) for widening their applications. To this end, we have chosen Zn<sup>II</sup> as a metal node for binding with TPY as such self-assembly is ubiquitously being explored due to soft acid-base interaction. We have performed titration of TPY-TTF (8 × 10<sup>-6</sup> M in MeOH) with a methanolic solution of Zn(NO<sub>3</sub>)<sub>2</sub>·6H<sub>2</sub>O (8 × 10<sup>-4</sup> M), and corresponding UV-Vis absorption spectra were recorded (Fig. 2b). Notably, the presence of isosbestic point in the Zn<sup>II</sup> titration suggested the complex formation between Zn<sup>II</sup> and TPY-TTF LMWG.<sup>54</sup> Job's plot analysis carried out using UV-Vis titration data illustrates the binding ratio of Zn(NO<sub>3</sub>)<sub>2</sub> and TPY-TTF is likely to be 2:1. Next, Zn(NO<sub>3</sub>)<sub>2</sub> and TPY-TTF gelator was taken in a molar ratio of 2:1 in the solvent mixture of MeOH/DCM/H<sub>2</sub>O (2:1:1). Heating the reaction mixture to 60 °C followed by cooling to room temperature has afforded a deep purple coloured coordination polymer gel (Zn-TPY-TTF CPG) (Fig. 2a, Supplementary Figs. 11–14). FESEM analysis of Zn-TPY-TTF showed entangled nanofibrous like morphology, suggesting metal coordination drastically changed the morphology in CPG (Fig. 2h). The length and diameter of nanofibres were found to be between 0.1 μm – 1 μm and 40-80 nm, respectively. Further, AFM images of Zn-TPY-TTF showed the height nanofibers was found to be ~7 nm (Figs. 2e-2g). The elemental mapping of the xerogel exhibited the uniform distribution of Zn<sup>II</sup> in a 3D network of the CPG (Supplementary Fig. 13). EDAX and elemental analyses also correlated the 2:1 ratio of Zn: TPY-TTF in the CPG (Supplementary Fig. 12). TEM studies also revealed similar morphologies as observed in FESEM and high-resolution TEM analysis exhibited ordering in the nanofibres and lattice fringes were observed with the distance of 3.6 Å which could be attributed to the intermolecular π-π stacking between the TTF and TPY from the [Zn(terpy)<sub>2</sub>] units (Fig. 2i-2j and 3a). Further, the PXRD pattern of Zn-TPY-TTF CPG showed a peak at 2θ = 24.9° (3.6 Å), justifying the presence of π-π stacking (Fig. 2d). The UV-Vis absorption spectrum of Zn-TPY-TTF in xerogel state was found to be similar to the TPY-TTF OG with a small bathochromic shift in the absorbance (+10 nm) as shown in Fig. 2c. The optical band gap for Zn-TPY-TTF was calculated to be 2.27 eV which is closer to the bandgap of TPY-TTF OG (Supplementary Fig. 9). Notably, TD-DFT calculations performed on Zn-TPY-TTF demonstrates a weak intramolecular CT (3%) at 568 nm (Supplementary Fig. 15b). At the same time, a strong intermolecular charge transfer (41%) from TTF core to terpyridine unit was observed at the same wavelength (568 nm) (Supplementary Fig. 15a) with additional intermolecular CT band at 588 nm (Fig. 3b). Intermolecular CT interactions could occur via π-π stacking, as supported by lattice fringes observed in the HR-TEM images. Importantly, terpyridine units in Zn-TPY-TTF were found to be more electron-deficient in nature and seem to be better electron acceptor as compared in TPY-TTF OG (Fig. 3b). Next, as a controlled study, we found energies of the LUMO for TTF(CONH<sub>2</sub>)<sub>4</sub> and [Zn(terpy)<sub>2</sub>] are -1.90 eV and -1.92 eV, respectively (Fig. 3c), which indicates that excited-state electron transfer is energetically favourable from TTF(CONH<sub>2</sub>)<sub>4</sub> core to [Zn(terpy)<sub>2</sub>] centre.

Next, Mott Schottky (MS) analysis was performed for the xerogel of both, TPY-TTF and Zn-TPY-TTF to evaluate experimental feasibility for water and CO<sub>2</sub> reduction (see SI for details). The MS plots exhibited n-type nature with a positive slope for both TPY-TTF and Zn-TPY-TTF (Fig. 4a). The flat band potentials ( $V_{fb}$ ) were found to be -0.60 V and -0.54 V versus RHE (at pH=7) for TPY-TTF and Zn-TPY-TTF, respectively. Based on the bandgaps obtained using UV-vis diffuse reflectance spectrometry (Supplementary Fig. 9), the electronic band structures versus RHE at pH 7 could be elucidated and are displayed in Fig. 4b.<sup>56</sup> Interestingly, the band alignments are shown in Fig. 4b illustrate that both TPY-TTF and Zn-TPY-TTF possess suitable band edge positions to perform water and CO<sub>2</sub> reduction under visible-light irradiation.

### **Photocatalytic activity under laboratory condition:**

#### **(a) Visible light driven photocatalytic H<sub>2</sub> production from water:**

We have examined the potential of CPG for photocatalytic H<sub>2</sub> production from water under visible light (400–750 nm) irradiation using 300 W xenon lamp as the light source (experimental details are given in the SI). Photocatalytic activity of Zn-TPY-TTF was examined in both, gel and xerogel state, and similar H<sub>2</sub> evolution was observed for both under similar conditions (Supplementary Fig. 16a). However, catalytic activities in different conditions were performed in the xerogel state because of ease handling of the catalyst in comparison to the gel state. After optimizing the catalyst loading (Supplementary Figs. 17), 1 mg of Zn-TPY-TTF in xerogel state was dispersed in 38 ml of water for the photocatalytic H<sub>2</sub> production, and 2 ml triethylamine (TEA) was added into it that acted as a sacrificial electron donor. The photocatalytic activity of Zn-TPY-TTF was monitored by gas chromatography (GC) analysis and showed 10.60 mmol/g of H<sub>2</sub> evolution in 20 h (activity =  $\sim 530 \mu\text{molg}^{-1}\text{h}^{-1}$ ) upon visible light irradiation. The amount of H<sub>2</sub> evolved was reached to saturation in 20 h and turnover number (TON) was calculated to be 23.5 (see SI) as shown in Fig. 4e. The activity is quite impressive and indeed higher than many other transition metal-based photocatalysts (Supplementary Tables 3-5). The Q.E. for H<sub>2</sub> production using Zn-TPY-TTF catalyst was calculated to be 0.76 % at 550 nm. Further, the absence of H<sub>2</sub> formation with Zn-TPY-TTF under dark condition (absence of light) confirming light is an essential component for the catalysis. Catalytic recyclability/reusability and stability are important factors to evaluate overall photocatalytic performance. To examine the recyclability, the photocatalytic study was performed with Zn-TPY-TTF for 6 h, and corresponding H<sub>2</sub> evolution was monitored (Supplementary Fig. 16b). After the first cycle, the reaction mixture was purged with N<sub>2</sub> gas for 30 minutes, and complete removal of the H<sub>2</sub> was ensured by the GC-analysis. Again, this reaction mixture was reused for photocatalysis, and this process was continued back and forth for four consecutive cycles. Interestingly, the amount of H<sub>2</sub> evolution was found to be similar in every cycle, confirming the excellent recyclability of the photocatalyst. Next, recycled catalyst (Zn-TPY-TTF) was analysed by FE-SEM and TEM studies and suggested no significant change in the structure and morphology after the catalytic reaction, indicating high stability of the catalyst (Supplementary Figs. 16c-d).

Next, we have examined photocatalytic activity for the OG to compare the importance of morphology, i.e., the spatial arrangement of the chromophore and also the role of metal directed assembly in CPG. Experimental conditions employed for the TPY-TTF OG was similar to the CPG. Interestingly, the H<sub>2</sub> evolution by the TPY-TTF OG upon visible light irradiation was increased exponentially and reached saturation in 22 h (Fig. 4e). The maximum H<sub>2</sub> evolution in 22h was calculated to be 2 mmol/g (activity~100 μmol g<sup>-1</sup>h<sup>-1</sup>), which is albeit lesser than the CPG but higher than the most of reported metal-free photocatalysts for H<sub>2</sub> evolution.<sup>57</sup>

To understand the significant difference in photocatalytic activities between TPY-TTF OG and Zn-TPY-TTF CPG, photocurrent measurements were performed for both (Fig. 4d) in the presence and absence of light. The photocurrent for Zn-TPY-TTF in the presence of light was found to be double as compared to TPY-TTF OG. This indicates the facile charge-separation in Zn-TPY-TTF under light irradiation; therefore, expected to show better photocatalytic activity as compared to TPY-TTF. This argument has further validated by the EIS measurement, where the charge transfer resistance for Zn-TPY-TTF was observed to be significantly lesser as compared to TPY-TTF under both, dark and light irradiated conditions (Fig. 4c). This can be attributed to the 1D nanofibril morphology of Zn-TPY-TTF CPG that provides a continuous charge transfer pathway (via co-facial intermolecular charge delocalization) for the photogenerated electrons which ultimately enhances the photocatalytic activity.

We have also performed the photocatalytic study with individual structural units of Zn-TPY-TTF as control experiments to evaluate the importance of coordination assembly of CPG in the catalysis (Supplementary Fig. 18). Notably, individual components such as TEA, TTF(COOH)<sub>4</sub> and TPY-TTF were found to be incapable of catalysing H<sub>2</sub> evolution reaction. Next, the photocatalytic study has also been performed by making a blend of Zn<sup>II</sup> salt with TPY-TTF (in 2:1 ratio) (details are given in SI). This showed aggregated spherical morphology as confirmed by FE-SEM study (Supplementary Fig. 19) and corresponding TON of H<sub>2</sub> evolution calculated for 6 h was found to be three-times lesser as compared to the CPG (Supplementary Fig. 18). This unambiguously signify the impact of nano-structuring in the photocatalytic performances. To validate the role of intermolecular CT interaction, we have also synthesized a coordination polymer of Zn<sup>II</sup> (Zn-CP) with TTF(COOH)<sub>4</sub> and characterized by FESEM, EDAX, elemental mapping, TGA, PXRD and UV-vis absorption study (Supplementary Figs. 20-23). Zn-CP showed micron-sized spherical particles with diameter in the range of 2-3 μm. The Zn-CP showed 0.8 mmol/g of H<sub>2</sub> production from water in 12 h which is eight times lesser in activity in comparison to Zn-TPY-TTF CPG photocatalyst under a similar condition. Overall, control experiments have unambiguously indicated that the coordination driven spatial arrangement of donor-acceptor charge transfer interaction has a high significance in visible light photocatalytic performances of CPG (Zn-TPY-TTF).

Further, we envisioned that the entangled hierarchical fibrous structure of the coordination polymer gels could easily immobilize co-catalyst like Pt on the surface<sup>58</sup>, which would facilitate the separation of photogenerated charge carriers by decreasing diffusion length and eventually enhance the photocatalytic activity.<sup>59</sup> Thus, we have successfully executed in-situ generation and stabilization of platinum (Pt)

nanoparticles in the 3D fibrous network of Zn-TPY-TTF (Pt@Zn-TPY-TTF) (Fig. 5a, see the details in SI). High-resolution TEM and FE-SEM analysis have confirmed for the stabilization of Pt nanoparticles in fibrous networks of Zn-TPY-TTF within the size range of 2-3 nm (Fig. 5b, Supplementary Fig. 24a). Lattice fringes were observed for Pt NPs with the d-spacing value of 0.23 nm, indicating the presence of Pt (111) planes (Fig. 5c). Inductively coupled plasma optical emission spectroscopy (ICP-OES) measurement and EDAX analysis indicated the presence of ~2.7 wt% Pt in Pt@Zn-TPY-TTF composite (Supplementary Fig. 24b). The elemental mapping was ensured for the uniform distribution of Pt NPs in the gel matrix (Supplementary Fig. 25). Next, photocatalytic activity towards water reduction was examined for Pt@Zn-TPY-TTF under similar condition as employed for CPG as well as OG. Interestingly, Pt@Zn-TPY-TTF has shown remarkably enhanced catalytic activity under visible light irradiation and hydrogen evolution was calculated to be 162.42 mmol/g in only 11 h (activity= $\sim 14727 \mu\text{mol g}^{-1}\text{h}^{-1}$ ) and corresponding TON value was found to be 360.1 (Fig. 5d). Drastically increased H<sub>2</sub> evolution after Pt nanoparticles stabilization could be ascribed to the efficient charge separation in Pt@Zn-TPY-TTF as Pt-centre is well-known electron acceptor that accumulate a pool of electrons and subsequently exhibits efficient water reduction. Thus, the gel matrix of Zn-TPY-TTF is primarily acting as a photosensitizer for the generation of photoexcited electrons which transferred to Pt nanoparticles to reduce water into H<sub>2</sub> using the harvested light energy. Furthermore, recyclability of Pt@Zn-TPY-TTF was evaluated in a continuous photocatalytic experiment performed for 24 h with intermittent H<sub>2</sub> evacuation by purging N<sub>2</sub> gas for 30 minutes in the time interval of 6 h (Supplementary Fig. 26b). This indicated for excellent catalytic recyclability as the catalytic performance after every 6 h was found to be almost similar. The Mott-Schottky analysis for Pt@Zn-TPY-TTF reveals that the conduction band edge occurs at -0.51 V vs. RHE at pH 7, which is lesser compared to the Zn-TPY-TTF CPG (-0.54 V) catalyst (Supplementary Fig. 27a). However, approximately four-folds higher photocurrent was observed for Pt@Zn-TPY-TTF as compared to Zn-TPY-TTF (Supplementary Fig. 27c), which further corroborated the facile electron transfer from the Zn-TPY-TTF to the Pt centre. The formation of Schottky junction in Pt@Zn-TPY-TTF was helpful to separate the photogenerated electron-hole pairs. This argument was further validated by the EIS measurement, where the charge transfer resistance for Pt@Zn-TPY-TTF was found to be almost half as compared to Zn-TPY-TTF under both, dark and visible light irradiation (Supplementary Fig. 27b). Further, the photoluminescence (PL) spectra of Zn-TPY-TTF showed weak emission with a maximum at 581 nm ( $I_{\text{ex}} = 520 \text{ nm}$ ) (Supplementary Fig. 28). PL spectra for Pt@Zn-TPY-TTF upon excitation at 520 nm showed significantly quenched emission as compared to Zn-TPY-TTF. Therefore, to gain more insight into the advantages of Pt NPs in the increased charge separation the time-resolved photoluminescence (TRPL) decay was studied on the Zn-TPY-TTF and Pt@Zn-TPY-TTF, as shown in Supplementary Fig. 29. A higher average lifetime Zn-TPY-TTF CPG system (1.95 ns) compared to Pt@Zn-TPY-TTF system (0.22 ns) obtained by the TRPL studies confirms that migration of photoexcited electrons is much faster in Pt@Zn-TPY-TTF compared to Zn-TPY-TTF.<sup>60,61</sup> The decrease in the lifetime is attributed to the enhanced separation and transfer efficiency of photogenerated electrons in Pt@Zn-TPY-TTF system, which plays decisive roles in enhancing the efficiency of photocatalytic processes. Furthermore, quantum efficiency (Q.E.) for the water reduction to H<sub>2</sub> was determined for the Pt@Zn-TPY-TTF upon irradiating with monochromatic light of the wavelength

of 400 nm, 450 nm, 500 nm, 550 nm, 600 nm, 650 nm and 700 nm (Supplementary Fig. 30). Notably, the highest Q.E. was obtained to be 14.47 % at 550 nm. This experiment is evident that the photocatalytic activity is mainly driven through intermolecular charge transfer interaction. The H<sub>2</sub> evolution using Pt@Zn-TPY-TTF was examined under both light and dark conditions (Supplementary Fig. S26c). No H<sub>2</sub> evolution was detected under dark condition, indicating the importance of light for the water reduction. Next, the photocatalysis was also performed for Pt@Zn-TPY-TTF and Zn-TPY-TTF CPG without any sacrificial donor (TEA). The aqueous dispersion of Zn-TPY-TTF produced 0.92 mmol/g of H<sub>2</sub> in 20 h and which is 11 times lesser than with TEA. Similarly, Pt@Zn-TPY-TTF showed 30 times lesser activity without TEA (Supplementary Table 3).

### **(b) Visible light driven photocatalytic CO<sub>2</sub> reduction:**

As mentioned above, the theoretical and experimental bandgap alignment of Zn-TPY-TTF CPG and TPY-TPY OG is in good agreement to reduce the CO<sub>2</sub> as well. Therefore, we have performed visible-light-driven photocatalytic CO<sub>2</sub> reduction studies with the xerogel of Zn-TPY-TTF and also compared with TPY-TTF OG. TEA was used as a sacrificial electron donor (SD) for CO<sub>2</sub> reduction (details are given in SI). First, screening of the solvent composition for CO<sub>2</sub> reduction has been performed (Supplementary Figs. 31-32) and mixture of acetonitrile: water (3:1) have shown the best activity. Visible light driven CO<sub>2</sub> reduction by Zn-TPY-TTF yielded 3.51 mmol/g of CO in 8 h with > 99% selectivity (activity= ~438 μmol g<sup>-1</sup> h<sup>-1</sup>). The Q.E. of CO<sub>2</sub> photoreduction for Zn-TPY-TTF CPG at 550 nm was calculated to be 1.71%. Such an impressive CO formation with outstanding selectivity is noteworthy and one of the best results among various reported hybrid photocatalysts systems (Supplementary Tables 6-8). The TON for Zn-TPY-TTF in 8 h was calculated to be 7.8 (Fig. 6b). The stability of Zn-TPY-TTF CPG was examined in the time interval of 6 h up to four cycles and found intact as for the first cycle, indicating the excellent catalytic stability (Supplementary Fig. 39a). Further, the photocatalytic activity of Zn-TPY-TTF was examined upon isotopic labelling with <sup>13</sup>CO<sub>2</sub> (see SI). This showed the formation of <sup>13</sup>CO, which confirms that the produced CO was originated from CO<sub>2</sub> (Supplementary Figs. 33-34). Next, visible light driven photocatalytic CO<sub>2</sub> reduction have also investigated for OG (TPY-TTF) under a similar condition as employed for Zn-TPY-TTF (Fig. 6a). The TPY-TTF has displayed 1.12 mmol/g CO formation in 11 h with >99% selectivity (activity= ~140 μmol g<sup>-1</sup> h<sup>-1</sup>) and corresponding TON was estimated to be 2.1 (Fig. 6a).

We have performed in situ Diffuse Reflectance Infrared Fourier Transform (DRIFT) spectroscopic study for Zn-TPY-TTF CPG to track the reaction intermediates formed in the course of CO<sub>2</sub> reduction to CO (see details in SI).<sup>56</sup> Two peaks appeared at 1514 and 1692 cm<sup>-1</sup> were assigned for the COOH\* and COO\* intermediates, respectively, which are the signature intermediates forms initially during the CO<sub>2</sub> reduction (Fig. 7a).<sup>62</sup> Peaks observed at 1454 cm<sup>-1</sup> could be attributed to symmetric stretching of the HCO<sub>3</sub>\*.<sup>63</sup> In addition, a peak at 1275 cm<sup>-1</sup> could be assigned for the C-OH\* of the HCO<sub>3</sub>\* intermediate.<sup>63</sup> A noteworthy peak at 2074 cm<sup>-1</sup> was indicated for formation of the CO\*. Most importantly, peak intensity of the CO\* intermediate was substantially increased with reaction progress, suggesting CO\* formation increases with

time. Based on the experimental results and in-situ study, we have computed plausible mechanism for CO<sub>2</sub> reduction which is in good agreement with earlier report as well<sup>27</sup> (Fig. 7b). The photocatalytic cycle is initiated by the light absorption at photosensitiser, which is TTF core followed by reductive quenching of TTF\* by TEA. Next, an electron generated from the TTF\* was transferred to [Zn(TPY)]<sup>2+</sup> and subsequently produced the radical cation species [Zn(TPY<sup>•-</sup>)(TPY)]<sup>1+</sup>. Notably, the electron was localized at terpyridine unit of the catalyst that resulted [Zn(TPY<sup>•-</sup>)(TPY)]<sup>1+</sup> species with the stabilization energy of 0.36 eV (Supplementary Fig. 43a). Next, as the reaction progress, a terpyridine ligand was leaving from the coordination sphere of Zn<sup>II</sup> and eventually solvent molecules (acetonitrile) occupy the vacant coordination site to afford a complex [Zn(TPY<sup>•-</sup>)(MeCN)<sub>2</sub>]<sup>1+</sup> (Supplementary Fig. 43b). This complex binds with a CO<sub>2</sub> molecule and produce the [Zn(TPY)(MeCN)<sub>2</sub>(CO<sub>2</sub><sup>-</sup>)]<sup>1+</sup> species (Supplementary Fig. 44d). As evidenced by the DFT results, Zn-CO<sub>2</sub> distance in the [Zn(TPY)(MeCN)<sub>2</sub>(CO<sub>2</sub><sup>-</sup>)]<sup>1+</sup> was decreased to 2.319 Å from 3.017 Å compared to transition state species (TS) (Supplementary Fig. 44c). Notably, CO<sub>2</sub> molecule acts as a monodentate ligand, and the angle for ∠O-C-O was found to be 140.75° keeping in mind that free CO<sub>2</sub> has linear geometry (Supplementary Fig. 44d). Here, it is worth mentioning that the one-electron charging over the [Zn-TPY] unit favours the binding of CO<sub>2</sub> molecule by increasing electron density at the metal centre, which is prerequisite for the nucleophilic attack to the CO<sub>2</sub>. However, the [Zn(TPY)(MeCN)<sub>2</sub>(CO<sub>2</sub><sup>-</sup>)]<sup>1+</sup> complex was further reduced to form the singlet species [Zn(TPY<sup>•-</sup>)(MeCN)<sub>2</sub>(CO<sub>2</sub><sup>-</sup>)] (Supplementary Fig. 44e). This carboxylate centre of the singlet complex reacts with the second molecule of CO<sub>2</sub> and subsequently releasing a carbonate anion from the catalytic cycle and resulting in the formation of [Zn(TPY)(MeCN)<sub>2</sub>(CO)]<sup>2+</sup> complex (Supplementary Fig. 44g). In this complex, the CO molecule is loosely attached to the Zn<sup>II</sup> centre at a distance of 2.585 Å. As a result, it can be easily released from the metal centre and therefore, catalyst molecule re-enters into the catalytic cycle.

Next, the photocatalytic activity of Pt@Zn-TPY-TTF towards CO<sub>2</sub> reduction has also been examined under a similar experimental condition as applied for CPG and OG. Pt@Zn-TPY-TTF is expected to show impressive catalytic activity due to the presence of Pt NPs. And indeed, this has depicted excellent CO<sub>2</sub> reduction and more interestingly, displayed CH<sub>4</sub> formation rather than CO (Fig. 6d). It has already been reported in the literature that the presence of Pt NPs on the surface of semiconductor plays a key role for the formation of CH<sub>4</sub>.<sup>58</sup> The low H<sub>2</sub> dissociation barrier and weak bond (H-Pt) facilitate the CO<sub>2</sub> bonding with hydrogen on the Pt surface.<sup>58,59,64</sup> Thus, Pt NPs acts as atomic hydrogen reservoir that supplies protons readily for CH<sub>4</sub> formation while CO<sub>2</sub> reduction. Screening of the solvent condition for Pt@Zn-TPY-TTF indicated that the maximum conversion of CO<sub>2</sub> to CH<sub>4</sub> can be achieved in the mixture of acetonitrile: water (3:1) (Supplementary Fig. 32). The formation of CH<sub>4</sub> was reached to saturation in 30 h and the corresponding yield was calculated to be 8.74 mmol/g (activity= ~292 μmol g<sup>-1</sup> h<sup>-1</sup>) (Fig. 6d). During CO<sub>2</sub> reduction, a small amount of H<sub>2</sub> evolution was also observed (~0.20 mmol/g in 30 h) which was more in the initial hours but significantly decreased as the reaction progressed with time. Thus, the selectivity of CO<sub>2</sub> reduction to CH<sub>4</sub> formation in 30 h was noted to be more than 97 % (Fig. 6e). The TON for CH<sub>4</sub> was

calculated to be 19.4 in 30 h, which is indeed impressive (Supplementary Table 8). The catalytic performance of Pt@Zn-TPY-TTF was examined for 6 h up to four cycles, and a similar amount of CH<sub>4</sub> formation in every cycle has ensured for excellent catalytic recyclability (Supplementary Fig. 39b). The quantum efficiency (Q.E.) of the Pt@Zn-TPY-TTF towards CO<sub>2</sub> reduction was calculated at different wavelengths using monochromatic light (Supplementary Fig. 37). The highest Q.E. for the CH<sub>4</sub> formation was obtained to be 0.81 % at 550 nm which further confirms that the photocatalytic activity of Pt@Zn-TPY-TTF is attributed to the intermolecular charge transfer interactions. The CO<sub>2</sub> reduction was also performed under both, light and dark conditions using Pt@Zn-TPY-TTF (Supplementary Fig. 38). The CH<sub>4</sub> formation was not increased under dark condition, justifying the importance of light in the photocatalysis. Further, photocatalysis was performed with labelled <sup>13</sup>CO<sub>2</sub> (isotopic labelling) using Pt@Zn-TPY-TTF (Supplementary Figs. 35-36). This showed the formation of labelled <sup>13</sup>CH<sub>4</sub> and confirming that CO<sub>2</sub> is the actual source for the CH<sub>4</sub> formation. Next, we have performed DRIFT experiment for Pt@Zn-TPY-TTF in order to monitor the real-time progress for the CO<sub>2</sub> reduction reaction (Fig. 8). Similar to the Zn-TPY-TTF, IR-stretching peaks observed for Pt@Zn-TPY-TTF at 1610 cm<sup>-1</sup>, 1570 cm<sup>-1</sup> and 1426 cm<sup>-1</sup> could be attributed to the intermediates COOH\*, COO\* and HCO<sub>3</sub>\*, respectively.<sup>56</sup> Weak intensity peak for the CO\* at 2062 cm<sup>-1</sup> illustrated that the CO\* could be readily converted to other multi-electron reduction intermediates. Moreover, the characteristic intermediates for CH<sub>4</sub> formation were observed at 1081 cm<sup>-1</sup> (CHO\*), 1015 and 1120 cm<sup>-1</sup> (CH<sub>3</sub>O\*).<sup>56</sup> This clearly showed that the presence of Pt NPs in the Pt@Zn-TPY-TTF CPG play catalytic role towards modulating the CO<sub>2</sub> reduction product from CO to CH<sub>4</sub>.

## Sunlight driven photocatalytic studies:

### (a) Sunlight driven H<sub>2</sub> evolution:

Above discussions have clearly shown that visible-light photocatalytic activity and stability of both, Zn-TPY-TTF and Pt@Zn-TPY-TTF in the xerogel state is indeed impressive. Notably, the amount of H<sub>2</sub> evolution obtained using photocatalyst Zn-TPY-TTF is higher than previously reported non-precious metal-based photocatalyst materials (Supplementary Table 5). Therefore, our next goal was to examine the potential of Zn-TPY-TTF towards H<sub>2</sub> evolution upon direct sunlight irradiation under ambient condition (Supplementary Fig. 40). Nevertheless, we have performed photocatalysis experiment with Zn-TPY-TTF in sunlight from 9:00 am to 4:00 pm for one week during 12<sup>th</sup> April 2019 – 17<sup>th</sup> April 2019 at the rooftop of our institute. The weather condition corresponding to the above-mentioned period can easily be found out on the web. Interestingly, maximum H<sub>2</sub> evolution of 5.14 mmol/g in 6 h (activity= ~857 μmol g<sup>-1</sup> h<sup>-1</sup>) upon direct sunlight irradiation was observed on 15<sup>th</sup> April which is quite impressive and indeed comparable with the amount of H<sub>2</sub> obtained under laboratory conditions (Xe-lamp irradiation). The TON for H<sub>2</sub> evolution was calculated for the above-mentioned period (Fig. 4f). The highest TON value of 11.9 was obtained on 15<sup>th</sup> April 2019. Whereas, the lowest TON was calculated to be 7.2 on 12<sup>th</sup> April

2019 because of partially cloudy weather. To the best of our knowledge, this work demonstrates the first example for the direct sunlight driven impressive H<sub>2</sub> evolution exploiting non-precious metal derived soft photocatalyst material.

Next, similar to Zn-TPY-TTF, we have also examined sunlight driven photocatalytic H<sub>2</sub> evolution for Pt@Zn-TPY-TTF composite in xerogel state (Fig. 5e). The experimental condition for Pt@Zn-TPY-TTF was similar to the Zn-TPY-TTF. Nevertheless, experimental timing was different for the Pt@Zn-TPY-TTF. The sunlight driven photocatalysis with Pt@Zn-TPY-TTF was performed from 27<sup>th</sup> June 2019 to 29<sup>th</sup> June 2019. Interestingly, water reduction efficiency of Pt@Zn-TPY-TTF under sunlight irradiation was extremely high. The highest H<sub>2</sub> evolution was calculated to be 72 mmol/g in 6 h (activity= ~12000 μmol g<sup>-1</sup> h<sup>-1</sup>) on 27<sup>th</sup> June 2019, and corresponding TON was calculated to be 159.7 (Fig. 5e). Whereas, the lowest TON value for H<sub>2</sub> evolution was found to be 114.6 on 28<sup>th</sup> June due to partially cloudy weather.

### **(b) Sunlight driven CO<sub>2</sub> reduction:**

Interestingly, the potential of Zn-TPY-TTF for CO<sub>2</sub> reduction has also been examined under direct sunlight between 9:00 a.m. to 4:00 pm for three days from 28<sup>th</sup> to 30<sup>th</sup> Sept 2019 (Fig. 6c). The highest CO formation of 1.79 mmol/g was observed in 6 h (activity= ~298 μmol g<sup>-1</sup> h<sup>-1</sup>) on 30<sup>th</sup> September 2019, and corresponding TON was calculated to be 3.9 (Fig. 6c). The CO formation under direct sunlight irradiation is albeit lower than the laboratory condition but the obtained amount under ambient condition is quite exciting and promising because of practical application.

Next, sunlight driven CO<sub>2</sub> reduction has been performed with Pt@Zn-TPY-TTF for three days from 1<sup>st</sup> October 2019 to 3<sup>rd</sup> October 2019 (Fig. 6f). Similar to the laboratory conditions, Pt@Zn-TPY-TTF composite upon sunlight irradiation has displayed CH<sub>4</sub> formation as the results of CO<sub>2</sub> reduction. The highest CH<sub>4</sub> formation of 0.96 mmol/g in 6 h (activity= ~160 μmol g<sup>-1</sup> h<sup>-1</sup>) was observed on 1<sup>st</sup> October 2019 and corresponding TON value was calculated to be 2.1. Whereas, the lowest CH<sub>4</sub> evolution with the TON value of 1.9 took place on 2<sup>nd</sup> October 2019. Furthermore, after performing sunlight driven photocatalysis with Zn-TPY-TTF CPG, the catalyst was recovered through centrifugation and washed with fresh water 3-4 times. The FE-SEM and TEM analysis performed for recovered catalyst sample has confirmed that the fibrous morphology of the Zn-TPY-TTF remained intact, whereas EDAX and elemental analysis ensured the presence of all the elements in similar quantity as obtained for as-synthesized Zn-TPY-TTF (Supplementary Fig. 41). This unambiguously demonstrates the excellent stability of the Zn-TPY-TTF CPG during sunlight irradiation. Similarly, the structural integrity of the recovered Pt@Zn-TPY-TTF after sunlight driven photocatalysis was analysed by microscopic techniques. FE-SEM & TEM images of recovered Pt@Zn-TPY-TTF was found to be similar to the as-synthesized material, indicating for excellent stability of the catalyst during photocatalysis (Supplementary Fig. 42).

## **Discussion**

In a nutshell, we have successfully demonstrated a TTF based soft processable metal-organic hybrid gel as a visible light photocatalyst for H<sub>2</sub> evolution and CO<sub>2</sub> reduction to carbonaceous fuel such as CO/CH<sub>4</sub>. The charge transfer driven photocatalyst based coordination polymer gel is the first of its kind, where earth-abundant metal ions play a crucial role in the spatial organization of donor-acceptor  $\pi$ -chromophores to drive the catalytic activity. Further, we have shown catalytic activity of the CPG after decorating Pt nanoparticles as co-catalyst. It enhances the rate of H<sub>2</sub> production in twenty-folds and dramatically changes the CO<sub>2</sub> reduction product from CO to CH<sub>4</sub>. We have also demonstrated efficient catalytic activity of the CPG and Pt decorated CPG under sunlight with high selectivity. The real-time reaction progress of CO<sub>2</sub> reduction was monitored by DRIFTS study and based on that; plausible mechanism of CO<sub>2</sub> reduction was elucidated for CPG. Easy processability and structural tunability of LMWG offers a lot of room towards designing efficient photocatalyst materials for practical application. Our work will pave the way toward designing new coordination driven hybrid soft processable photocatalyst systems for solar energy driven fuel production.

## References

1. Banerjee, T., Gottschling, K., Savasci, G., Ochsenfeld, C. & Lotsch, B. V. H<sub>2</sub> Evolution with Covalent Organic Framework Photocatalysts. *ACS Energy Lett.* **3**, 400–409 (2018).
2. Wang, Y. *et al.* Current Understanding and Challenges of Solar Driven Hydrogen Generation using Polymeric Photocatalysts. *Nat. Energy* **4**, 746–760 (2019).
3. Windle, C. D. *et al.* Earth-Abundant Molecular Z–Scheme Photoelectrochemical Cell for Overall Water-Splitting. *J. Am. Chem. Soc.* **141**, 9593–9602 (2019).
4. Andrei, V., Reuillard, B. & Reisner, E. Bias-Free solar Syngas Production by Integrating A Molecular Cobalt Catalyst with Perovskite–BiVO<sub>4</sub> Tandems. *Nat. Mater.* **19**, 189–194 (2020).
5. Alkhatib, I. I., Garlisi, C., Pagliaro, M., Ali, K. A. & Palmisano, G. Metal-Organic Frameworks for Photocatalytic CO<sub>2</sub> Reduction Under Visible Radiation: A Review of Strategies and Applications. *Catal. Today* **340**, 209–224 (2020).
6. Ge, J., Zhang, Y. & Park, S. J. Recent Advances in Carbonaceous Photocatalysts with Enhanced Photocatalytic Performances: A Mini Review. *Materials* **12**, 1916–1942 (2019).
7. Montoya, A. T. & Gillan, E. G. Enhanced Photocatalytic Hydrogen Evolution from Transition-Metal Surface-Modified TiO<sub>2</sub>. *ACS Omega* **3**, 2947–2955 (2018).
8. Kim, W., McClure, B. A., Edri, E. & Frei, H. Coupling Carbon Dioxide Reduction with Water Oxidation in Nanoscale Photocatalytic Assemblies. *Chem. Soc. Rev.* **45**, 3221–3243 (2016).
9. Reisner, E. When Does Organic Photoredox Catalysis Meet Artificial Photosynthesis? *Angew. Chem. Int. Ed.* **58**, 3656–3657 (2019).
10. Kornienko, N., Zhang, J. Z., Sakimoto, K. K., Yang, P. & Reisner, E. Interfacing Nature's Catalytic Machinery with Synthetic Materials for Semi-Artificial Photosynthesis. *Nat. Nanotechnol.* **13**, 890–899 (2018).

11. Niu, J., Albero, J., Atienzar, P. & Garcia, H. Porous Single-Crystal-Based Inorganic Semiconductor Photocatalysts for Energy Production and Environmental Remediation: Preparation, Modification, and Applications. *Adv. Funct. Mater.* **30**, 1908984–1909035 (2020).
12. Dhakshinamoorthy, A., Asiri, A. M. & Garcia, H. 2D Metal–Organic Frameworks as Multifunctional Materials in Heterogeneous Catalysis and Electro/Photocatalysis. *Adv. Mater.* **31**, 1900617–1900657 (2019).
13. Leung, J. J., Vigil, J. A., Warnan, J., Moore, E. E. & Reisner, E. Rational Design of Polymers for Selective CO<sub>2</sub> Reduction Catalysis. *Angew. Chem. Int. Ed.* **58**, 7697 – 7701 (2019).
14. Sokol, K. P. *et al.* Reversible and Selective Interconversion of Hydrogen and Carbon Dioxide into Formate by a Semiartificial Formate Hydrogenlyase Mimic. *J. Am. Chem. Soc.* **141**, 17498–17502 (2019).
15. Appel, A. M. *et al.* Frontiers, Opportunities, and Challenges in Biochemical and Chemical Catalysis of CO<sub>2</sub> Fixation. *Chem. Rev.* **113**, 6621–6658 (2013).
16. Qiao, J., Liu, Y., Hong, F. & Zhang, J. A Review of Catalysts for the Electroreduction of Carbon Dioxide to Produce Low-Carbon Fuels. *Chem. Soc. Rev.* **43**, 631–675 (2014).
17. Huang, Q. *et al.* Multielectron Transportation of Polyoxometalate-Grafted Metalloporphyrin Coordination Frameworks for Selective CO<sub>2</sub>-to-CH<sub>4</sub> Photoconversion. *Natl. Sci. Rev.* **7**, 53–63 (2020).
18. Albero, J., Peng, Y. & Garcia, H. Photocatalytic CO<sub>2</sub> Reduction to C<sub>2</sub> + Products. *ACS Catal.* **10**, 5734–5749 (2020).
19. Cometto, C. *et al.* A Carbon Nitride/Fe Quaterpyridine Catalytic System for Photostimulated CO<sub>2</sub>-to-CO Conversion with Visible Light. *J. Am. Chem. Soc.* **140**, 7437–7440 (2018).
20. Chang, X., Wang, T. & Gong, J. CO<sub>2</sub> Photo-Reduction: Insights Into CO<sub>2</sub> Activation and Reaction on Surfaces of Photocatalysts. *Energy Environ. Sci.* **9**, 2177–2196 (2016).
21. Dalle, K. E. *et al.* Electro- and Solar-Driven Fuel Synthesis with First Row Transition Metal Complexes. *Chem. Rev.* **119**, 2752–2875 (2019).
22. Twilton, J. *et al.* The Merger of Transition Metal and Photocatalysis. *Nat. Rev. Chem.* **1**, 52 (51 – 19) (2017).
23. Zhang, X. *et al.* Delocalized Electron Effect on Single Metal Sites in Ultrathin Conjugated Microporous Polymer Nanosheets for Boosting CO<sub>2</sub> Cycloaddition. *Sci. Adv.* **6**, eaaz4824 (4821 – 4810) (2020).
24. Oshima, T. *et al.* Undoped Layered Perovskite Oxynitride Li<sub>2</sub>LaTa<sub>2</sub>O<sub>6</sub>N for Photocatalytic CO<sub>2</sub> Reduction with Visible Light. *Angew. Chem. Int. Ed.* **57**, 8154 – 8158 (2018).
25. Miller, M. *et al.* Interfacing Formate Dehydrogenase with Metal Oxides for the Reversible Electrocatalysis and Solar-Driven Reduction of Carbon Dioxide. *Angew. Chem. Int. Ed.* **58**, 4601–4605 (2019).
26. Gao, C. *et al.* Co<sub>3</sub>O<sub>4</sub> Hexagonal Platelets with Controllable Facets Enabling Highly Efficient Visible-Light Photocatalytic Reduction of CO<sub>2</sub>. *Adv. Mater.* **28**, 6485–6490 (2016).

27. Kuehnel, M. F., Orchard, K. L., Dalle, K. E. & Reisner, E. Selective Photocatalytic CO<sub>2</sub> Reduction in Water through Anchoring of a Molecular Ni Catalyst on CdS Nanocrystals. *J. Am. Chem. Soc.* **139**, 7217–7223 (2017).
28. Bera, R., Dutta, A., Kundu, S., Polshettiwar, V. & Patra, A. Design of a CdS/CdSe Heterostructure for Efficient H<sub>2</sub> Generation and Photovoltaic Applications. *J. Phys. Chem. C* **122**, 12158–12167 (2018).
29. Ulmer, U. *et al.* Fundamentals and Applications of Photocatalytic CO<sub>2</sub> Methanation. *Nat. Commun.* **10**, 3169, 3161–3112 (2019).
30. Rao, H., Lim, C. H., Bonin, J., Miyake, G. M. & Robert, M. Visible-Light-Driven Conversion of CO<sub>2</sub> to CH<sub>4</sub> with an Organic Sensitizer and an Iron Porphyrin Catalyst. *J. Am. Chem. Soc.* **140**, 17830–17834 (2018).
31. Takeda, H. *et al.* Highly Efficient and Robust Photocatalytic Systems for CO<sub>2</sub> Reduction Consisting of a Cu(I) Photosensitizer and Mn(I) Catalysts. *J. Am. Chem. Soc.* **140**, 17241–17254 (2018).
32. Feng, X. *et al.* Metal – Organic Frameworks Significantly Enhance Photocatalytic Hydrogen Evolution and CO<sub>2</sub> Reduction with Earth-Abundant Copper Photosensitizers. *J. Am. Chem. Soc.* **142**, 690–695 (2020).
33. Gao, C. *et al.* Heterogeneous Single-Atom Photocatalysts: Fundamentals and Applications. *Chem. Rev.* <https://dx.doi.org/10.1021/acs.chemrev.9b00840> (2020).
34. Liu, D., Wan, J., Pang, G. & Tang, Z. Hollow Metal–Organic-Framework Micro/Nanostructures and their Derivatives: Emerging Multifunctional Materials. *Adv. Mater.* **31**, 1803291–1803308 (2019).
35. Zhang, G. *et al.* Tailoring the Grain Boundary Chemistry of Polymeric Carbon Nitride for Enhanced Solar Hydrogen Production and CO<sub>2</sub> Reduction. *Angew. Chem. Int. Ed.* **58**, 3433 – 3437 (2019).
36. Sutar, P. & Maji, T. K. Coordination Polymer Gels: Soft Metal–Organic Supramolecular Materials and Versatile Applications. *Chem. Commun.* **52**, 8055–8074 (2016).
37. Zhao, F., Bae, J., Zhou, X., Guo, Y. & Yu, G. Nanostructured Functional Hydrogels as an Emerging Platform for Advanced Energy Technologies. *Adv. Mater.* **30**, 1801796–1801812 (2018).
38. Samanta, D., Verma, P., Roy, S. & Maji, T. K. Nanovesicular MOF with Omniphilic Porosity: Bimodal Functionality for White-Light Emission and Photocatalysis by Dye Encapsulation. *ACS Appl. Mater. Interfaces* **10**, 23140–23146 (2018).
39. Kazantsev, R. V. *et al.* Crystal-Phase Transitions and Photocatalysis in Supramolecular Scaffolds. *J. Am. Chem. Soc.* **139**, 6120–6127 (2017).
40. Weingarten, A. S. *et al.* Self-Assembling Hydrogel Scaffolds for Photocatalytic Hydrogen Production. *Nature Chem* **6**, 964–970 (2014).
41. Sutar, P., Suresh, V. M., Jayaramulu, K., Hazra, A. & Maji, T. K. Binder Driven Self-Assembly of Metal–Organic Cubes Towards Functional Hydrogels. *Nat. Commun.* **9**, 3587, 3581 – 3512 (2018).
42. Wu, H. *et al.* Metallogels: Availability, Applicability, and Advanceability. *Adv. Mater.* **31**, 1806204–1806227 (2019).

43. Savyasachi, A. J. *et al.* Supramolecular Chemistry: A Toolkit for Soft Functional Materials and Organic Particles. *Chem* **3**, 764–811 (2017).
44. Kim, J. H., Nam, D. H., Lee, Y. W., Nam, Y. S. & Park, C. B. Self-Assembly of Metalloporphyrins into Light-Harvesting Peptide Nanofiber Hydrogels for Solar Water Oxidation. *small* **10**, 1272–1277 (2014).
45. Kong, K. *et al.* A Self-Assembled Perylene Diimide Nanobelt for Efficient Visible-Light-Driven Photocatalytic H<sub>2</sub> Evolution. *Chem. Commun.* **55**, 8090–8093 (2019).
46. Yang, L. *et al.* Donor – Acceptor Supramolecular Organic Nanofibers as Visible-Light Photoelectrocatalysts for Hydrogen Production. *ACS Appl. Mater. Interfaces* **10**, 19764–19772 (2018).
47. Sun, J., Schmidt, B. V. K. J., Wang, X. & Shalom, M. Self-Standing Carbon Nitride-Based Hydrogels with High Photocatalytic Activity. *ACS Appl. Mater. Interfaces* **9**, 2029–2034 (2017).
48. Weingarten, A. S. *et al.* Supramolecular Packing Controls H<sub>2</sub> Photocatalysis in Chromophore Amphiphile Hydrogels. *J. Am. Chem. Soc.* **137**, 15241–15246 (2015).
49. Maiti, B., Abramov, A., Ruiz, R. P. & Diaz, D. D. The Prospect of Photochemical Reactions in Confined Gel Media. *Acc. Chem. Res.* **52**, 1865–1876 (2019).
50. Nalluri, S. K. M. *et al.* Conducting Nanofibers and Organogels Derived from the Self-Assembly of Tetrathiafulvalene-Appended Dipeptides. *Langmuir* **30**, 12429–12437 (2011).
51. Guasch, J. *et al.* Induced Self-Assembly of a Tetrathiafulvalene-Based Open-Shell Dyad through Intramolecular Electron Transfer. *Angew. Chem. Int. Ed.* **51**, 11024 – 11028 (2012).
52. Jana, A. *et al.* Tetrathiafulvalene- (TTF-) Derived Oligopyrrolic Macrocycles. *Chem. Rev.* **117**, 2641–2710 (2017).
53. Lu, M. *et al.* Rational Crystalline Covalent Organic Frameworks Design for Efficient CO<sub>2</sub> Photoreduction with H<sub>2</sub>O. *Angew. Chem. Int. Ed.* **58**, 12392 – 12397 (2019).
54. Sutar, P., Suresh, V. M. & Maji, T. K. Tunable Emission in Lanthanide Coordination Polymer Gels Based on A Rationally Designed Blue Emissive Gelator. *Chem. Commun.* **51**, 9876–9879 (2015).
55. Mitamura, Y., Yorimitsu, H., Oshima, K. & Osuka, A. Straightforward Access to Aryl-Substituted Tetrathiafulvalenes by Palladium-Catalysed Direct C–H Arylation and Their Photophysical and Electrochemical Properties. *Chem. Sci.* **2**, 2017–2021 (2011).
56. Li, X. *et al.* Selective Visible-Light-Driven Photocatalytic CO<sub>2</sub> Reduction to CH<sub>4</sub> Mediated by Atomically Thin CuIn<sub>5</sub>S<sub>8</sub> Layers. *Nat. Energy* **4**, 690–699 (2019).
57. Rahman, M. Z., Kibria, M. G. & Mullins, C. B. Metal-Free Photocatalysts for Hydrogen Evolution. *Chem. Soc. Rev.* **49**, 1887–1931 (2020).
58. Fu, J., Jiang, K., Qiu, X., Yu, J. & Liu, M. Product Selectivity of Photocatalytic CO<sub>2</sub> Reduction Reactions. *Mater. Today* **32**, 222–243 (2020).

59. Wang, W. N. *et al.* Size and Structure Matter: Enhanced CO<sub>2</sub> Photoreduction Efficiency by Size-Resolved Ultrafine Pt Nanoparticles on TiO<sub>2</sub> Single Crystals. *J. Am. Chem. Soc.* **134**, 11276–11281 (2012).
60. Xie, S. *et al.* Visible Light-Driven C – H Activation and C–C Coupling of Methanol into Ethylene Glycol. *Nat. Commun.* **9**, 1181 (1181–1187) (2018).
61. Ou, H., Chen, X., Lin, L., Fang, Y. & Wang, X. Biomimetic Donor–Acceptor Motifs in Conjugated Polymers for Promoting Exciton Splitting and Charge Separation. *Angew. Chem. Int. Ed.* **57**, 8729–8733 (2018).
62. Liang, L. *et al.* Infrared Light-Driven CO<sub>2</sub> Overall Splitting at Room Temperature. *Joule* **2**, 1004–1016 (2018).
63. Zhang, R. *et al.* Photocatalytic Oxidative Dehydrogenation of Ethane Using CO<sub>2</sub> as a Soft Oxidant over Pd/TiO<sub>2</sub> Catalysts to C<sub>2</sub>H<sub>4</sub> and Syngas. *ACS Catal.* **8**, 9280–9286 (2018).
64. Xie, S., Wang, Y., Zhang, Q., Deng, W. & Wang, Y. MgO- and Pt-Promoted TiO<sub>2</sub> as an Efficient Photocatalyst for the Preferential Reduction of Carbon Dioxide in the Presence of Water. *ACS Catal.* **4**, 3644–3653 (2014).

## Scheme

Scheme 1 is available in the Supplementary Files.

## Figures

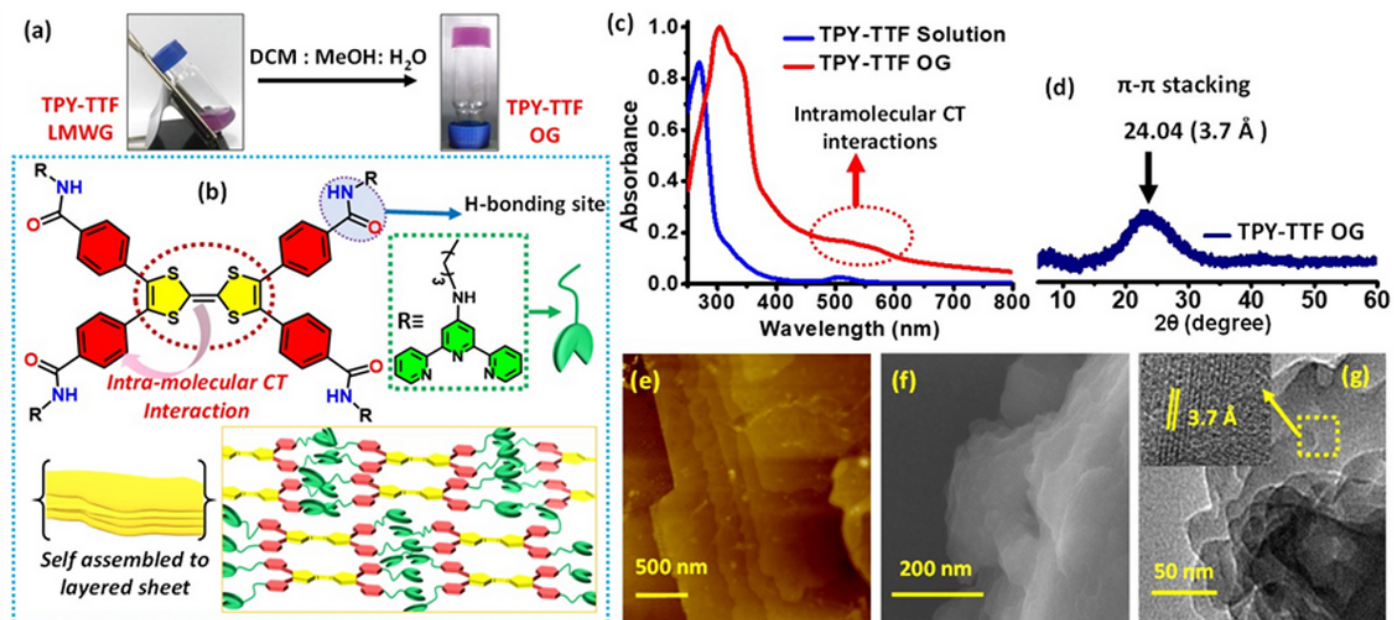


**Figure 1**

Synthesis and characterization of organogel. (a) Photograph of TPY-TTF organogel formation. (b) Pictorial representation for self-assembly of TPY-TTF LMWG forming layered sheet like morphology. (c) Absorption spectra of TPY-TTF in solution and gel state. (d) PXRD pattern of TPY-TTF xerogel. Morphology of TPY-TTF xerogel (e) AFM image; (f) FESEM image. (g) HR-TEM image (inset: showing lattice fringes).

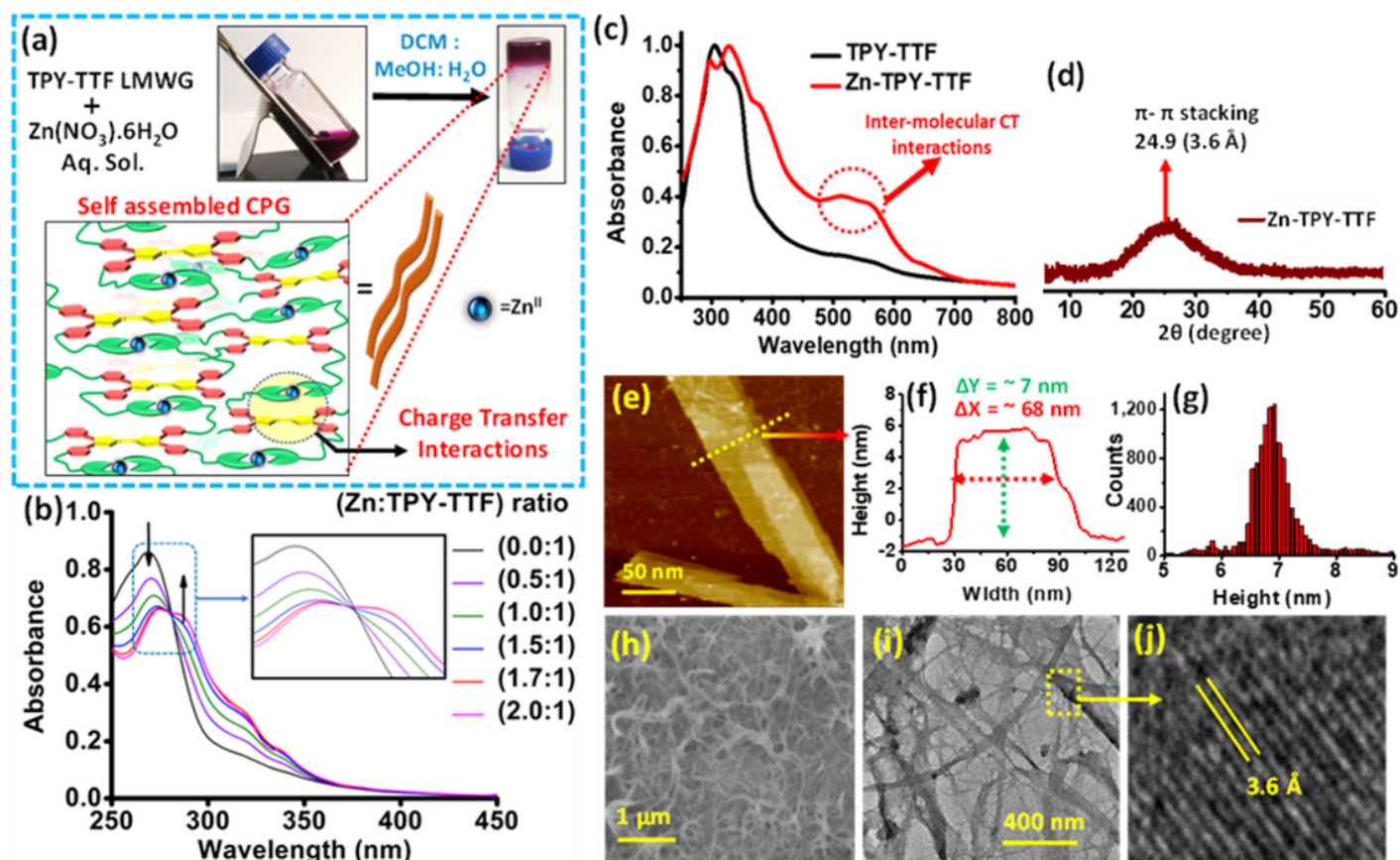


**Figure 2**

Synthesis and characterization of Zn-TPY-TTF CPG. (a) Photograph of Zn-TPY-TTF CPG formation and schematic representation for self-assembly of Zn-TPY-TTF CPG. (b) Titration of TPY-TTF LMWG with ZnII ion. (c) Solid state absorption spectra of TPY-TTF (black) and Zn-TPY-TTF (red). (d) PXRD of Zn-TPY-TTF xerogel. (e) AFM images of Zn-TPY-TTF xerogel. (f) Height profile of ribbon-like structure. (g) Height histogram. (h) FESEM image of Zn-TPY-TTF xerogel. (i) HRTEM image of Zn-TPY-TTF xerogel. (j) lattice fringes of Zn-TPY-TTF of the selected region.

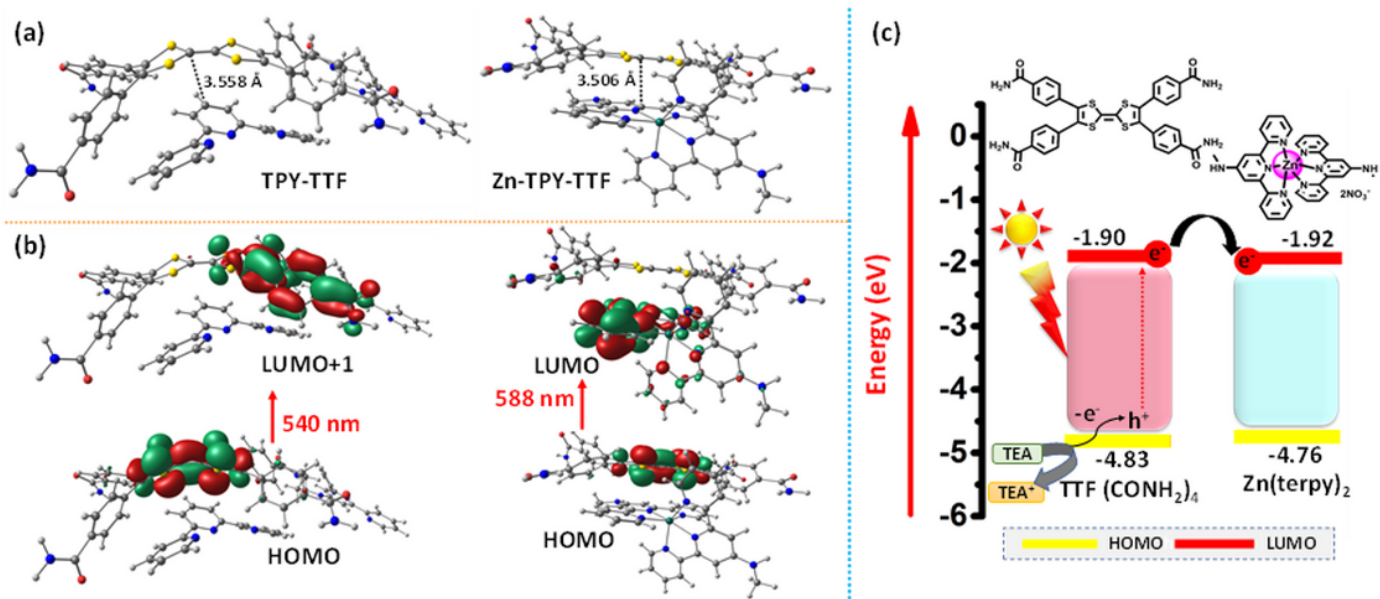
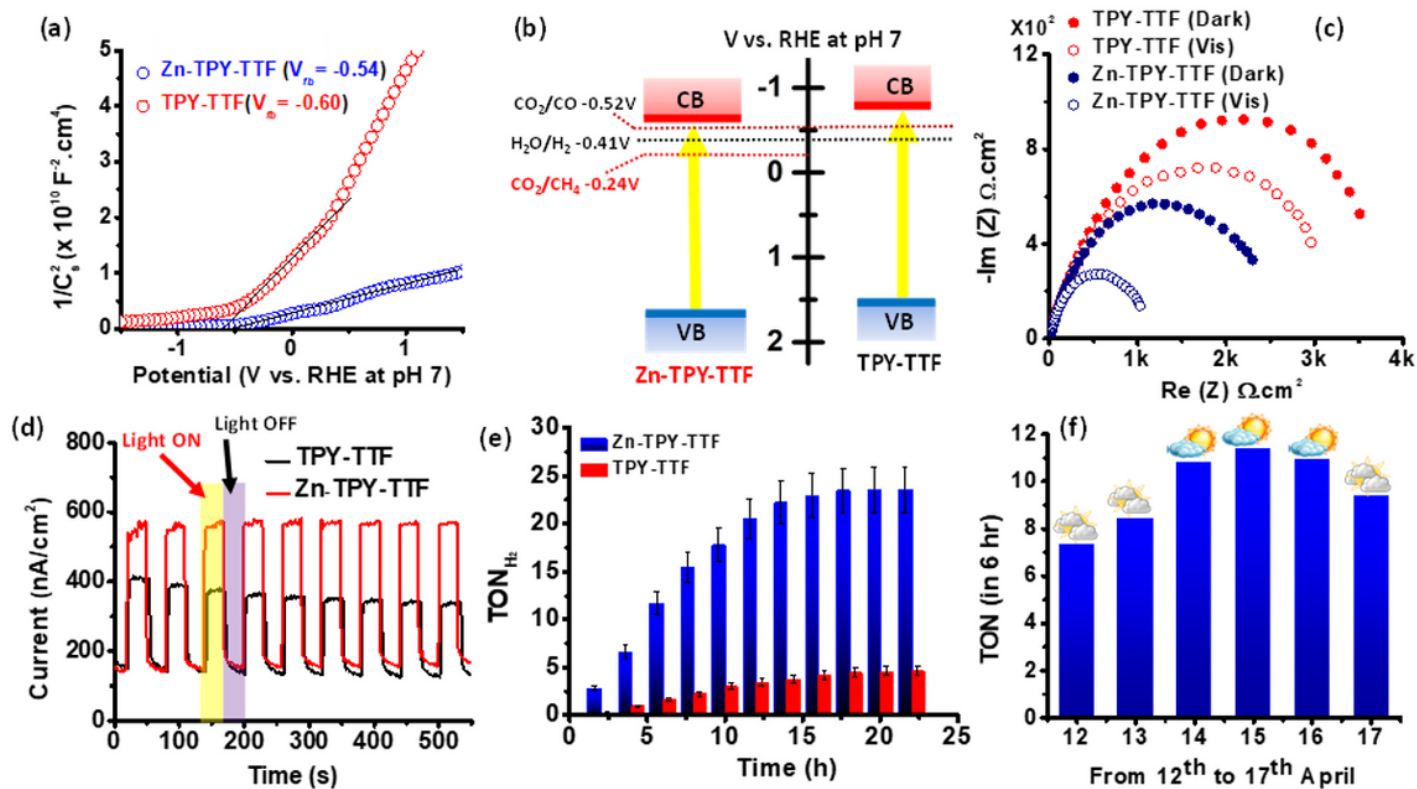


Figure 3

DFT calculations for CT interaction in TPY-TTF OG and Zn-TPY-TTF CPG. (a) Optimized structure of TPY-TTF and Zn-TPY-TTF; (b) HOMO-LUMO charge transfer transitions for TPY-TTF OG and Zn-TPY-TTF CPG; (c) HOMO-LUMO band alignments of TTF(CONH)<sub>4</sub> and Zn(terpy)<sub>2</sub> for thermodynamic feasibility of electron transfer.



**Figure 4**

Electrochemical characterization and photocatalytic H<sub>2</sub> production performances. (a) Mott Schottky plot for TPY-TTF and Zn-TPY-TTF w.r.t. RHE at pH=7 (at 1000 Hz, -1.5 V to +1.5 V). (b) Band alignment for TPY-TTF and Zn-TPY-TTF based on Mott Schottky plot (V vs. RHE at pH=7). (c) Nyquist plot for TPY-TTF and Zn-TPY-TTF under light and dark condition. (d) Photocurrent measurement for TPY-TTF and Zn-TPY-TTF in 0.5 M Na<sub>2</sub>SO<sub>4</sub> at + 0.8 V, pH=6.8 upon visible light irradiation in the time interval of 30 sec. (e) TON (for H<sub>2</sub>) value for Zn-TPY-TTF and TPY-TTF under laboratory condition. (f) TON value of H<sub>2</sub> evolution for Zn-TPY-TTF under direct sunlight irradiation from 12th to 17th April 2019 (9 am to 16 pm).

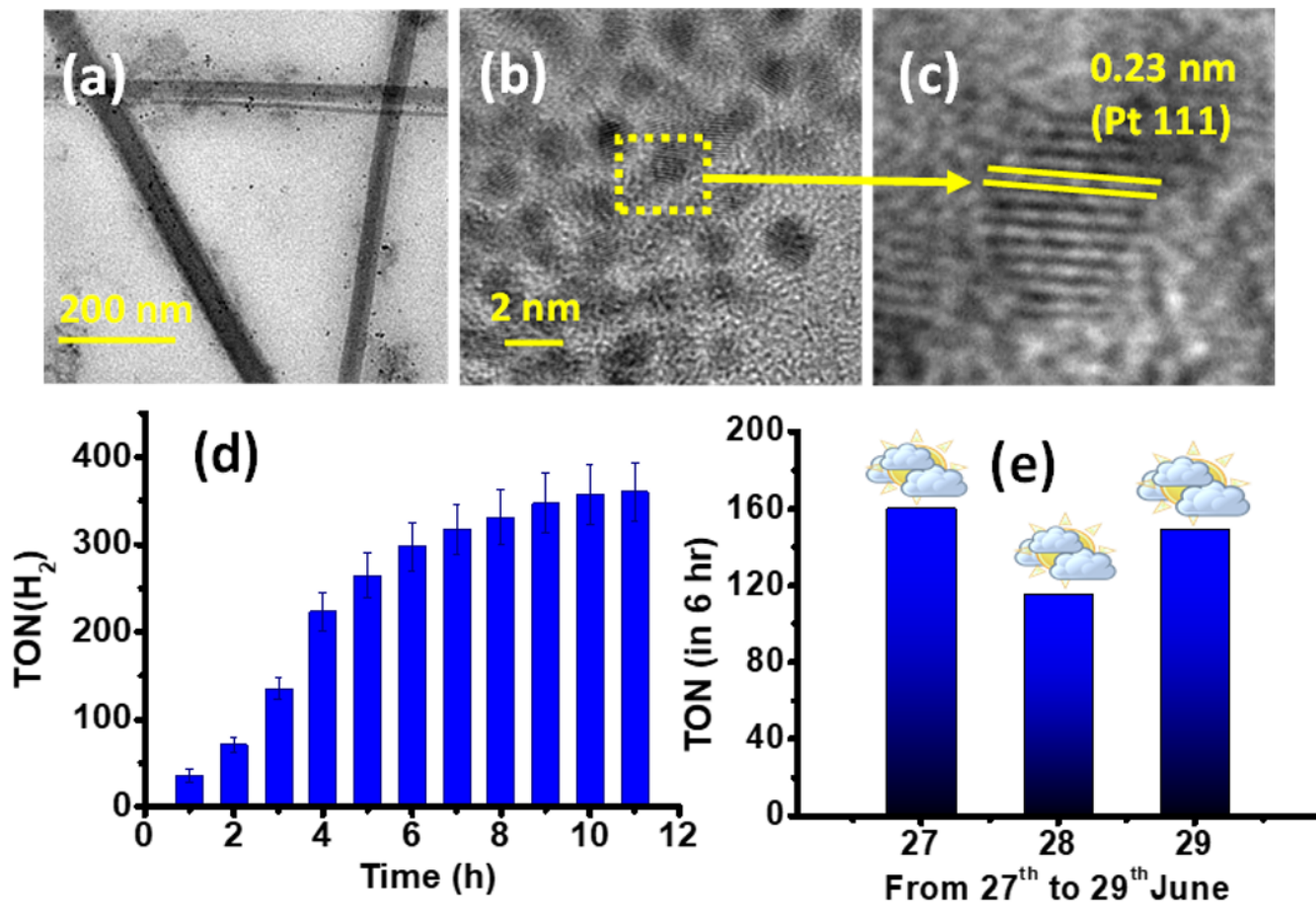


**Figure 5**

Characterization of Pt@Zn-TPY-TTF and photocatalytic activity for water reduction. (a-c) TEM images of Pt@Zn-TPY-TTF composite. (d) TON for H<sub>2</sub> evolution under visible light irradiation (> 420 nm). (e) TON for H<sub>2</sub> evolution for Pt@Zn-TPY-TTF composite under direct sunlight irradiation from 27th June to 29th June 2019 (9 am to 4 pm).

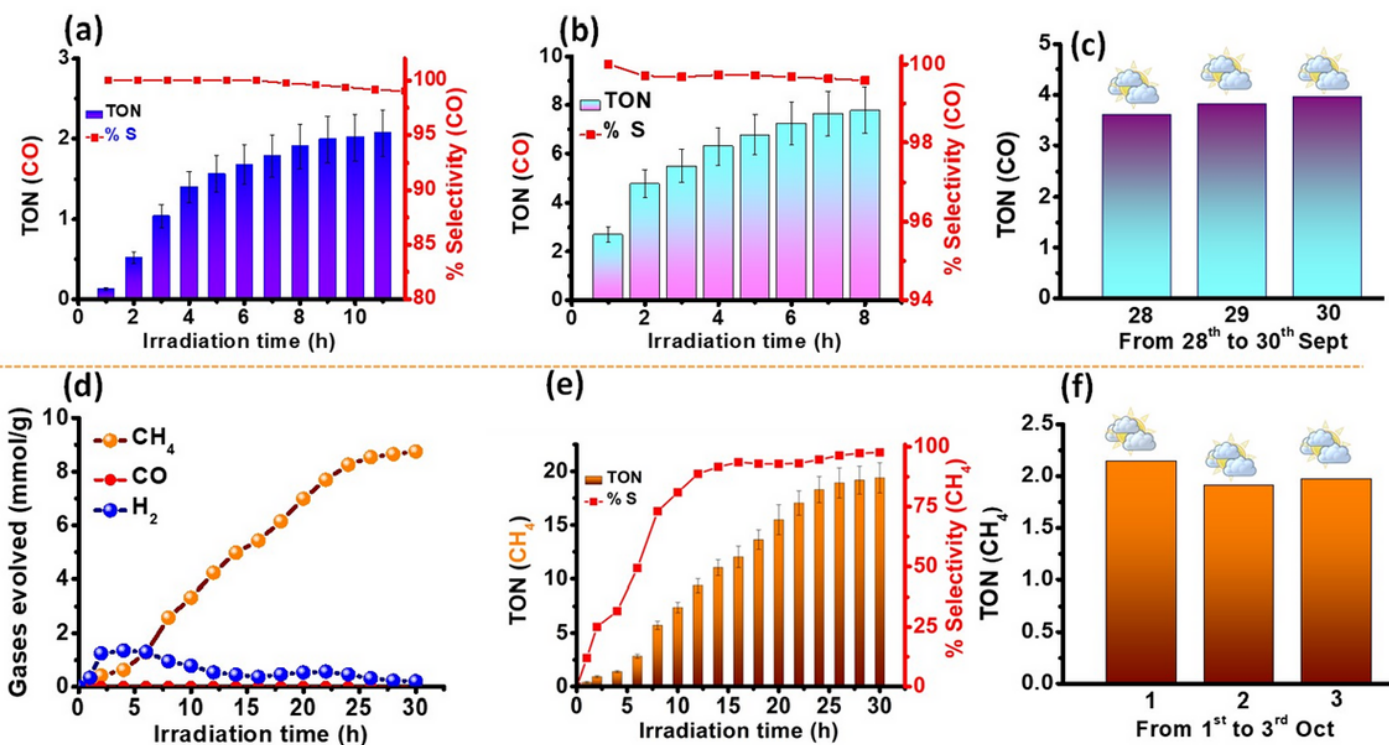


Figure 6

Photocatalytic CO<sub>2</sub> reduction under visible light/sunlight irradiation. (a) In the presence of TPY-TTF OG (TON for CO formation and selectivity). (b) In the presence of Zn-TPY-TTF CPG (TON for CO formation and selectivity). (c) TON for CO formation under sunlight from 28th Sept to 30th Sept 2019 in the presence of Zn-TPY-TTF CPG. (d) CO<sub>2</sub> reduction by Pt@ Zn-TPY-TTF composite (amount of CH<sub>4</sub> and H<sub>2</sub> formation with increasing time). (e) TON value and % selectivity for CH<sub>4</sub> formation using Pt@ Zn-TPY-TTF composite. (f) TON for CH<sub>4</sub> formation from CO<sub>2</sub> upon sunlight irradiation from 1st Oct to 3rd Oct 2019 in the presence of Pt@ Zn-TPY-TTF composite.

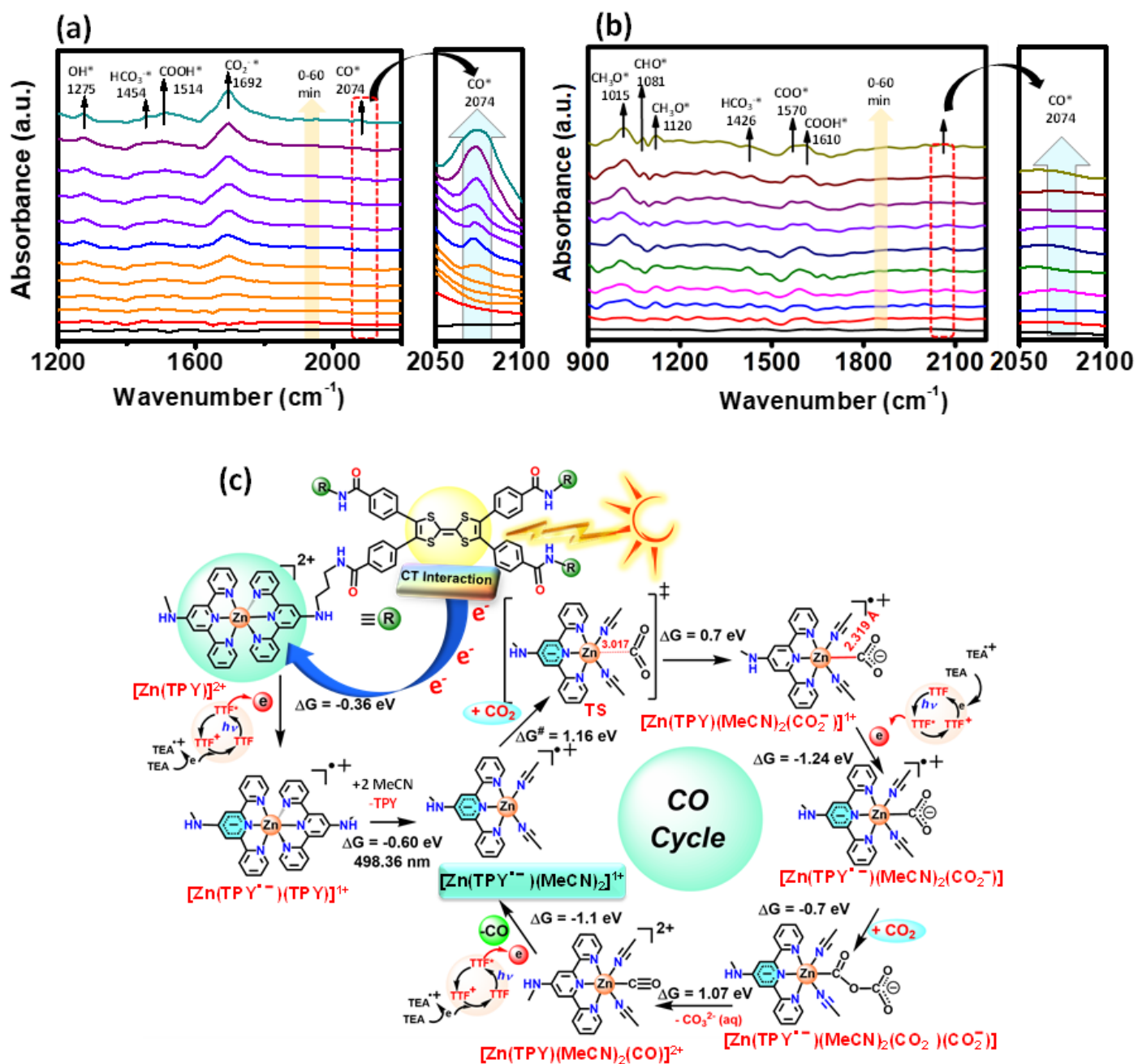


Figure 7

Real-time monitoring and plausible mechanism for CO<sub>2</sub> reduction. (a) In situ DRIFTS spectra for photocatalytic CO<sub>2</sub> reduction by Zn-TPY-TTF CPG. (b) In-situ DRIFTS spectra for photocatalytic CO<sub>2</sub> reduction by Pt@Zn-TPY-TTF CPG. (c) Plausible mechanism based on theoretical study for CO<sub>2</sub> reduction to CO by Zn-TPY-TTF CPG.

## Supplementary Files

This is a list of supplementary files associated with this preprint. Click to download.

- [SupportingInformation.docx](#)
- [Scheme1.png](#)